

# In-Situ Synthesis of —P=N-Doped Carbon Nanofibers for Single-Atom Catalytic Hydrosilylation

Liyuan Zhang,\* Hange Zhang, Kairui Liu,\* Jing Hou, Bolortuya Badamdorj, Nadezda V. Tarakina, Mengran Wang, Qiyu Wang, Xiaohan Wang, and Markus Antonietti

Single-atom catalysts have become a popular choice in various catalysis applications, as they take advantages of both homogeneous catalysis (e.g., high efficiency) and heterogeneous catalysis (e.g., easy catalyst recovery). The atom support plays an indispensable role in anchoring atomic species and interplaying with them for ultimate catalytic performance. Therefore, development of new support materials for superior catalysis is of great importance. Here the synthesis of carbon nanofibers based on the reaction between phosphorus pentoxide (P<sub>2</sub>O<sub>5</sub>) and *N*-methyl-2-pyrrolidone (NMP) is reported. The underlying reaction process is systematically investigated by Fourier-transform infrared (FTIR) spectroscopy and nuclear magnetic resonance (NMR) spectroscopy. The carbon nanofibers have interesting —P=N— units in their chemical structure, which act as anchoring sites for the single-atom catalyst. The Pt atoms anchoring carbon nanofibers exhibit high activity for hydrosilylation with a turnover frequency (TOF) of  $9.2 \times 10^6 \text{ h}^{-1}$  and a selectivity of >99%. This research affords not only a new in situ chemical strategy to synthesize multiatom doped carbon nanofibers but also presents a potential superior support in catalysis, which opens a hopeful window in materials chemistry and catalysis applications.

possess high electric conductivity, improved chemical & physical stability, and ultrahigh mass transfer efficiency. Therefore, in the past several decades, 1D carbon nanostructures have been exploited as robust materials in catalysis,<sup>[2]</sup> either as active materials or functional matrices to anchor various metal species.<sup>[3]</sup> To improve the application potential, introduction of heteroatoms into the 1D carbon nanostructure is essential as it allows to effectively engineer the electronic structure.<sup>[4]</sup> P and N are the popular choices but incorporating these heteroatoms into 1D carbon nanostructures normally needs multiple synthetic steps. It is important to develop simple and controllable method to synthesize heteroatom-doped 1D carbon nanostructures with superior abilities in cutting-edge applications.

Alkene hydrosilylation is the addition of Si—H to the unsaturated bonds, which is one of the most important chemical

reactions to produce the organosilicon compounds. Platinum (Pt) homogeneous catalysts, namely the Speier Pt catalyst and Karstedt Pt catalyst,<sup>[5]</sup> have been the most popular choice in alkene hydrosilylation<sup>[6]</sup> and consume nearly 5.6 tons of platinum annually in silicone industry.<sup>[7]</sup> Unfortunately, the side reactions, including the alkene isomerization and dehydrogenative silylation, normally accompany with the main reaction, and expensive purification is needed.<sup>[8]</sup> Moreover, the additional side reactions occur due to the formation of colloidal Pt species,<sup>[9]</sup> and the recycling of Pt homogeneous catalyst is a well-known challenge. This not only increases the production cost but also introduces impurities to the final product.<sup>[10]</sup> In this context, single-atom catalysts, which contains atomic dispersion of active metallic species on a support, have been recently developed to overcome these challenges. It exhibits an unexpected catalytic performance, while it also owns great convenience in recovery. The synthesis of the atom support is the key step to obtain this interesting material.

More recently, based on P<sub>2</sub>O<sub>5</sub> chemistry, we successfully synthesized metal-free C—O—P functionalized carbon-nanofiber assemblies.<sup>[11]</sup> This unique carbon nanostructure was proven to possess exceptional adsorption properties, a useful pre-requirement for catalysis. The outcome further inspired us to upgrade this in situ P<sub>2</sub>O<sub>5</sub> chemistry to introduce novel functional groups to 1D carbon nanostructure. Unfortunately, the previously

## 1. Introduction

1D carbon nanostructures have attracted major attention since their first discovery in 1991.<sup>[1]</sup> Typically, 1D carbon nanostructures

L. Zhang, H. Zhang, K. Liu, J. Hou, B. Badamdorj, N. V. Tarakina, M. Antonietti

Max Planck Institute of Colloids and Interfaces  
Department of Colloid Chemistry  
14476 Potsdam, Germany

E-mail: atomic\_liyuan@yeah.net; kairui.liu@kaust.edu.sa

L. Zhang, M. Wang, Q. Wang  
School of Metallurgy and Environment  
Central South University  
Changsha 410083, P. R. China

X. Wang  
School of Minerals Processing and Bioengineering  
Central South University  
Changsha 410083, P. R. China

 The ORCID identification number(s) for the author(s) of this article can be found under <https://doi.org/10.1002/adma.202209310>.

© 2023 The Authors. Advanced Materials published by Wiley-VCH GmbH. This is an open access article under the terms of the Creative Commons Attribution-NonCommercial-NoDerivs License, which permits use and distribution in any medium, provided the original work is properly cited, the use is non-commercial and no modifications or adaptations are made.

DOI: 10.1002/adma.202209310

employed starting product, plant oil, mainly contains C, H, and O in its chemical structure, based on which it is impossible to achieve in situ chemical synthesis of P,N co-doped carbon nanofibers. As the amide linkage  $=O=C-N$  is related to the ester linkage of plant oils,  $=O=C-O$ , we herein performed control experiments where similar carbon nanofibers assemblies with N and P co-doping were achieved when using N-methyl-2-pyrrolidone (NMP) as carbon source. The mechanism was investigated by analyzing the intermediates with Fourier-transform infrared (FTIR) and nuclear magnetic resonance (NMR) techniques. Moreover, the crucial factors affecting the formation of carbon nanofibers were disclosed. The carbon nanofibers assemblies include the  $-N=P$  unit/group within their chemical structures and thereby provide many anchoring sites for single atoms, while keeping them isolated. As such, the P,N co-doped carbon nanofibers were grafted with Pt atoms and applied to the hydrosilylation reactions. Super-high activity (TOF as high as  $9.2 \times 10^6 \text{ h}^{-1}$ ) with high selectivity (>99%) was achieved by using the catalyst, which can be attributed to the atomic dispersion of electron deficient  $Pt_1$  atoms.

## 2. Results and Discussion

### 2.1. Synthesis of Carbon Nanofibers

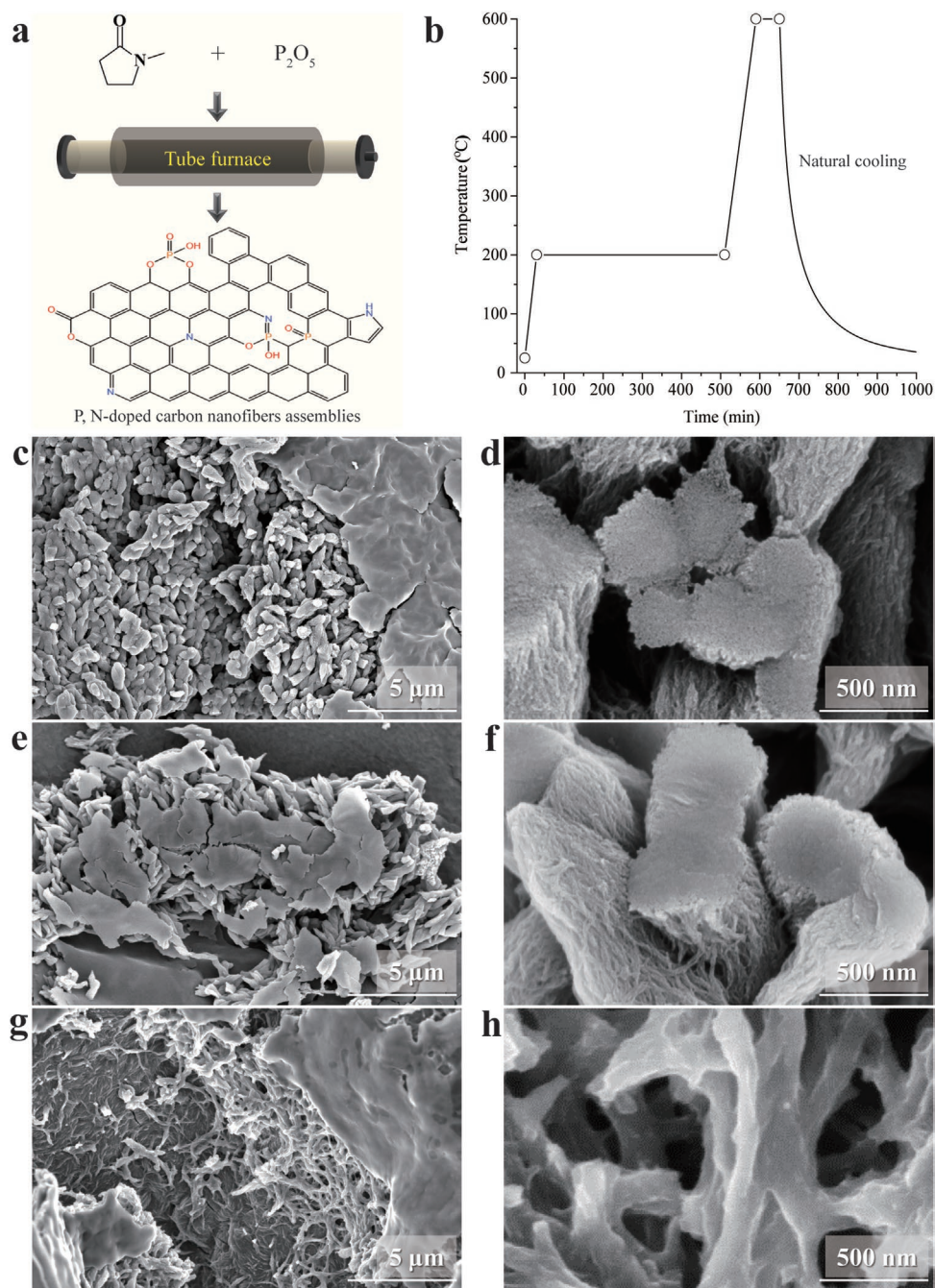
In a typical synthesis, the  $P_2O_5$  powder was added into NMP solution, and the mixture was heat-treated in tube furnace in  $N_2$  atmosphere following a set program (Figure 1a,b). After washing and drying, a black carbon powder with N and P doping was obtained. The products were named as  $C_{NP-x}$ , where  $x$  represents the carbonization temperature ( $^{\circ}C$ ). Scanning electron microscopy (SEM) was taken to see the morphology, and the temperature obviously affected the final morphology of the carbon nanostructures. As shown in Figure 1c–e, the majority of  $C_{NP-500}$  and  $C_{NP-600}$  are carbon nanofiber assemblies. As indicated from the cross-section image of  $C_{NP-500}$  (Figure 1d) and  $C_{NP-600}$  (Figure 1f), the fibers are assembled together in a relatively loose manner. The carbon nanofibers assemblies are in addition covered with a secondary structure – carbon nanosheets forming a sheath. For  $C_{NP-700}$  (Figure 1g,h), the original carbon nanofibers seem to further fuse together to form much bigger fiber bundles standing on thick carbon sheets.

### 2.2. Possible Reaction Process

To understand the reaction process, the intermediates were synthesized by selecting different temperatures at 200, 300, and 400  $^{\circ}C$ . The intermediates are denoted as intermediate- $x$ , where  $x$  represents the reaction temperature ( $^{\circ}C$ ). As shown in Figure S1 (Supporting Information), the intermediate-200 is a hard, red solid, while the intermediate-300 becomes black, porous, and brittle. The intermediate-400 is very similar to the final carbon product. The intermediate-200 is completely soluble in water. With the increase of temperature, the solubility of the intermediate in water decreases. This is quite different from the intermediates prepared by  $P_2O_5$ -plant oil reaction at 200  $^{\circ}C$ ,

which is nearly insoluble to any solvents. This interesting phenomenon possibly indicates that the oligomerization occurs at relatively low temperature, while the oligomer gradually polymerizes by increasing the reaction temperature.

The structure of the intermediate was investigated by FTIR and NMR techniques to elucidate the morphology evolution. Figure 2a provides the FTIR spectra of the intermediates, which includes the assignment of major functional groups. As seen, the  $HC=C-O$  and  $P-O-C$  ( $800-1000 \text{ cm}^{-1}$ ) are found in all intermediates, but the relative content of  $HC=C-O$  decreases with increasing temperature. Noticeably, it is found that there are  $C-O-C=C$  and  $C-N-P=O$  (overlapped between  $1000-1300 \text{ cm}^{-1}$ ) in all intermediates,<sup>[12]</sup> which are absent in  $P_2O_5$ -plant oil intermediates.<sup>[11]</sup> Moreover, the IR spectrum of intermediate-400 changes obviously after removing the soluble part. As shown in Figure 2a, the insoluble part of intermediate-400 contains relatively high content of  $P-O-C$  and relatively low content of  $HC=C-O$ . Moreover, for the insoluble part, the  $C=O$  disappears, and the two peaks are located in the range of  $1000-1300 \text{ cm}^{-1}$  red shift, which might correspond to the decreased content of  $HC=C-O$ . These data most possibly indicate that the  $HC=C-O$  and  $C=O$  mainly existed in the water-soluble fragment of the intermediates (or oligomers part of intermediates). Based on the structural fragments from FTIR analysis, the possible structure of the intermediate is provided in Figure 2c. As illustrated in Figure 2c, the oligomers, typically the trimers, were formed due to the cyclization of ketene, which is also in line with the previous research.<sup>[13]</sup> The decreased content of  $HC=C-O$  when increasing the reaction temperature is possibly due to the polymerization through double bond to form the cross-linked structure. This can also explain the declined solubility of intermediate-300 and -400 in water. Figure 2b shows the NMR spectra of intermediate-200. As seen in  $^1H$ -NMR spectrum, the  $HC-O$  ( $\approx 3.6 \text{ ppm}$ ),  $O-C=CH$  ( $\approx 4.3 \text{ ppm}$ ), and  $C=CH-CH_3$  ( $\approx 3.5 \text{ ppm}$ ) could be found. Moreover, the  $^{13}C$ -NMR spectrum demonstrates the  $O=C$  ( $\approx 178 \text{ ppm}$ ),  $C-O$  ( $\approx 63 \text{ ppm}$ ), and  $O-C=CH-$  ( $\approx 168 \text{ ppm}$  and  $\approx 101 \text{ ppm}$ , respectively) in intermediate-200. In addition, the phosphoric acid ( $\approx 0 \text{ ppm}$ ),  $O=P-O$  ( $\approx -11.5 \text{ ppm}$ ), and  $O=P-N/N=P-O$  ( $< 20 \text{ ppm}$ , P(III)) could be found in  $^{31}P$ -NMR spectrum. Totally speaking, the NMR analysis matches the FTIR analysis very well. Interestingly, based on the NMR analysis, a major part of the P(V) was chemically transformed into P(III), and the phosphoric acid is generated by the reaction between residual  $P_2O_5$  in the intermediate and  $D_2O$ . The elemental analysis of the final product indicates the formula of  $H_2C_{4.4}N_{0.24}O$ . As compared to the formula of NMP ( $H_9C_5NO$ ), the elimination products can be accounted as  $H_7C_{0.6}N_{0.8}$ . That means abundant reduction products are liberated throughout the reaction NMP, and that  $P_2O_5$  can act under reaction conditions as an oxidation agent, while being itself reduced from P(V)-oxide to P(III)-nitride. The formation of the carbon nanofibers is possibly derived from the “ketene-like polymerization” of the intermediate, followed by carbonization. Additionally, the effect of the structure of diverse starting monomers on the carbon morphology was investigated, including different chain length and functional groups. Results indicated that both the chain length and functional groups heavily affect the morphology of the carbon materials (Figures S2 and S3, Supporting Information).



**Figure 1.** a,b) Illustration of the synthesis of N, P-doping carbon nanofibers. c–h) SEM images of the carbon materials: c,d)  $C_{NP-500}$ , e,f)  $C_{NP-600}$ , and g,h)  $C_{NP-700}$ .

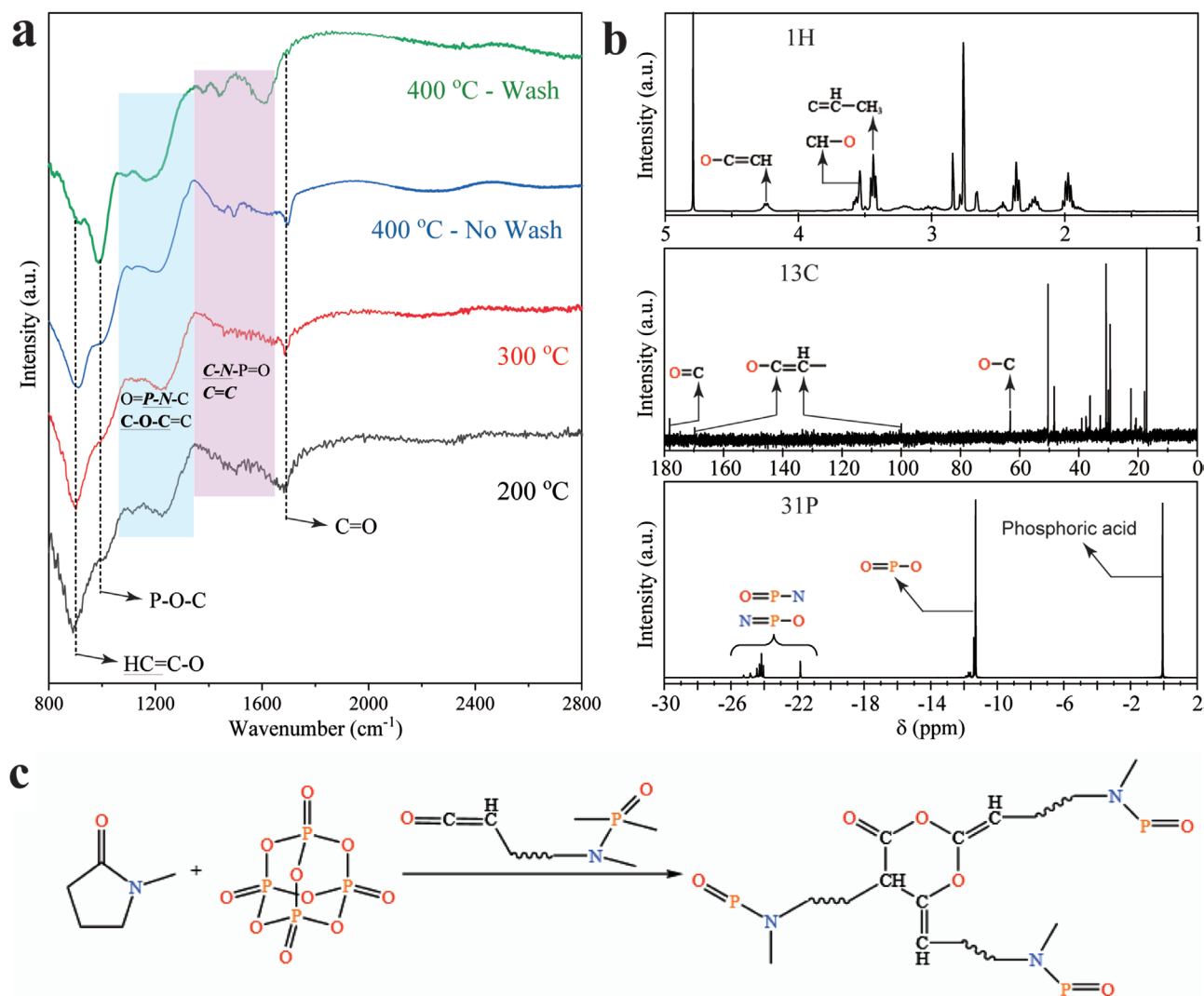
### 2.3. Characterizations of the Carbon Nanofibers

High-resolution transmission electron microscopy (HRTEM) was used to investigate the carbon nanofibers assemblies. As shown in Figure 3a,b, the carbon nanofibers ( $C_{NP-500}$  and  $C_{NP-600}$ ) assembled with relatively loose contact. However, when the carbonization temperature increased to 700 °C, the carbon nanofibers completely fused into much bigger sub-microfibers (Figure S4, Supporting Information). This is in consistence with the above SEM results that increasing the temperature would be

conductive to triggering the fusion of carbon nanofibers. Based on the elemental mapping (Figure 3c,d; Figure S4, Supporting Information), the C, N, P, and O could be clearly seen on the carbon materials, which demonstrates the N and P co-doping on the carbon nanofibers. Typically, the N and P account for  $\approx 4$  and  $\approx 6$  at% of the total element, respectively.

Furthermore, X-ray photoelectron spectroscopy (XPS) was used to see the heteroatoms doping in carbon nanofibers by taking  $C_{NP-600}$  as a typical example (Figure 3e–h). As seen in the survey spectrum in Figure 3e, the carbon materials contain



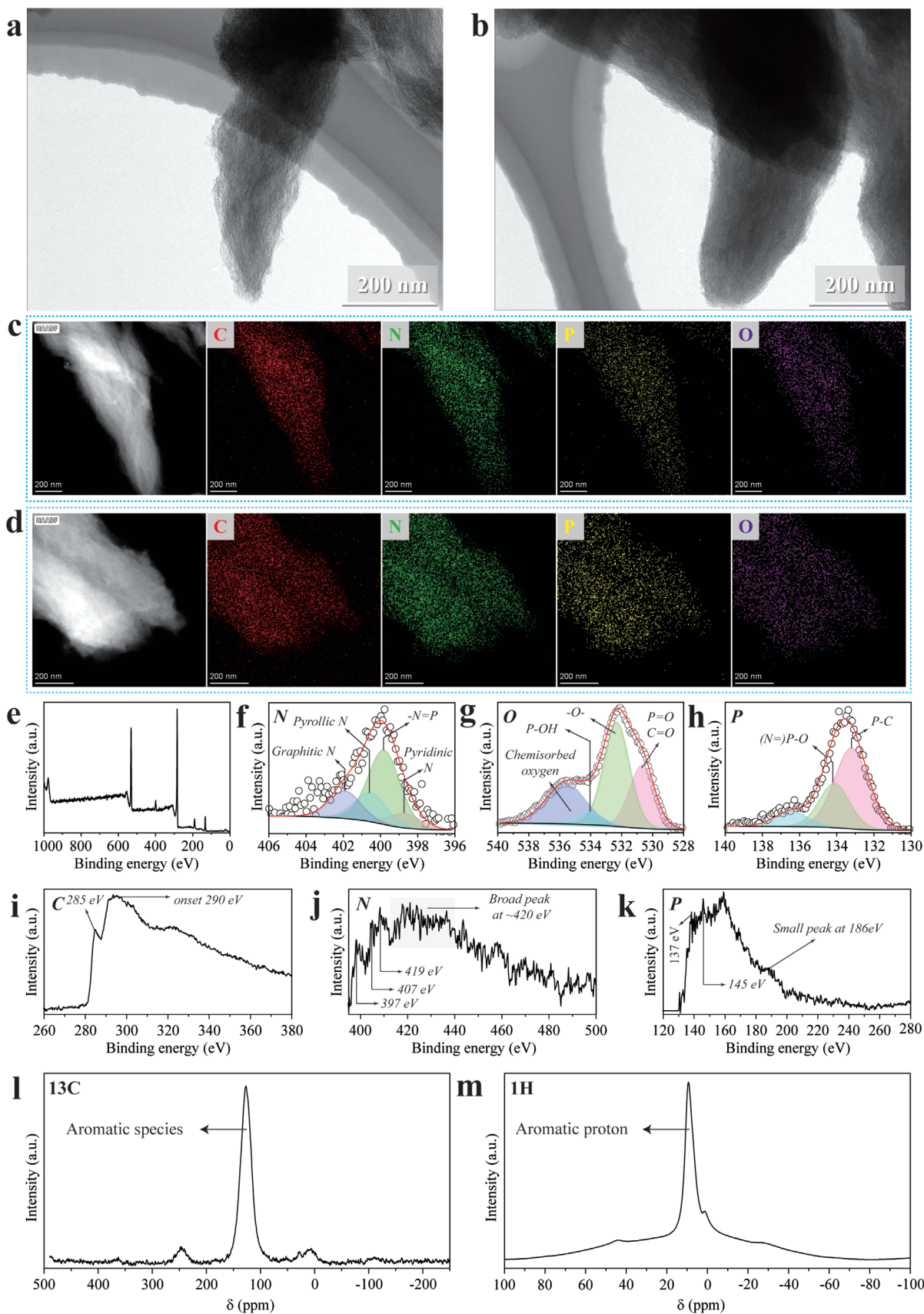


**Figure 2.** Characterization of the  $P_2O_5$ -NMP intermediates: a) FTIR spectra, b) liquid-state NMR spectra of intermediate-200, c) possible reaction pathways.

C, N, O, and P, which confirms the P,N co-doping in the final materials. The atomic content of N and P is 4.85 and 7.54 at%, respectively. The deconvolution of N, O, and P provides more information on these heteroatoms. Figure 3f presents the N1s spectrum of  $C_{NP}$ -600. The well-known components like pyridinic-N ( $\approx 398.8$  eV), pyrrolic-N ( $\approx 400.5$  eV), and graphitic-N ( $\approx 401.9$  eV) are all found here.<sup>[14]</sup> However, the peak center in Figure 3f is at  $\approx 399.9$  eV, which is different from most of the previous reported spectra. Based on previous empirical research,<sup>[15]</sup> the  $-P=N$  units with P connecting to electrophiles such as O-based groups exhibit the peak at  $\approx 399.8$  eV, which could explain the XPS N1s spectrum. To the best of our knowledge, this interesting  $-N=P$  doping is rare in carbon materials. This kind of doping could be further proved with the deconvolution of O1s (Figure 3g) and P2p (Figure 3h) spectra. Noticeably, another P doping is in the form of P-C bond in carbon structure. Differing from the carbon nanofibers synthesized by  $P_2O_5$ -plant oil, the  $C_{NP}$ -600 absorbed a certain amount of adsorbed oxygen, which might be due to the different, very

oxyphilic structures in this material. The effect of temperature (500 and 700 °C, in Figures S5 and S6, Supporting Information respectively) on the doping conditions was investigated by XPS, too, which shows no significant difference to  $C_{NP}$ -600.

To further confirm the formation of  $-N=P-$  doping, electron energy loss spectroscopy (EELS) was applied to detect the electronic structure of  $C_{NP}$ -600. As given in Figure 3i, C-K edge shows the characteristic maximum at 285 eV induced by the transitions of the electrons to  $\pi^*$  molecular orbital, and the second broad peak with onset at 290 eV corresponds to transitions to  $\sigma^*$  orbitals.<sup>[16]</sup> Three peaks at 397, 407, and 419 eV at N-K edge (Figure 3j) correspond to the  $\pi^*$  and the two  $\sigma^*$  peaks, similar to the spectra of pyridine-like nitrogen.<sup>[16,17]</sup> Moreover, as referred to the previous study, the P-L<sub>2,3</sub> edge at 137 and 145 eV (Figure 3k) suggests the presence of  $-N=P-O$  in the carbon materials;<sup>[18]</sup> while the P-L<sub>2,3</sub> edge at 183 eV (Figure 3k) is related to the presence of P=N coordination.<sup>[19]</sup> Another two different positions were selected to get the EELS spectra to confirm the uniform distribution of the chemical



structures (Figure S7, Supporting Information). In summary, the EELS analysis is in good agreement with the XPS analysis. In addition, the C–K edge gives us a relative indication of electron delocalization in the carbon structure, and aromatization seems to be restricted, as typical for such low synthetic temperatures. This is confirmed by solid-state NMR on the main product. As seen in Figure 3l,m, the carbon material is mainly made up of all C–C  $sp^2$  C, so-called graphitic carbon.

Raman was taken to analyze the samples. As shown in Figure S8 (Supporting Information), the G peak ( $\approx 1601\text{ cm}^{-1}$ ) and D peak ( $\approx 1372\text{ cm}^{-1}$ ) could be found in all three samples. The  $I_D/I_G$  is  $\approx 0.99$  for these samples, usually related to a relatively good graphitization degree, but we also point to the fact that both P- and N doping also bring vibrational dissymmetry and thereby apparent disorder. On the other hand, the thermal stability of the carbon materials was studied by thermogravimetric analysis (TGA). As seen in Figure S9 (Supporting Information), an obvious thermal decomposition occurred when the temperature reached  $500\text{ }^\circ\text{C}$ , which is in line with the previous research, but also the tendency towards nanotube fusion observed for the higher temperature samples. Nevertheless, this indicates a good performance in thermal stability to plan potential catalytic experiments, even when compared with carbon nanotubes (Figure S9, Supporting Information).<sup>[11]</sup> In the X-ray diffraction (XRD) pattern (Figure S10, Supporting Information), the samples behave as typical carbons with low long-range translational order, but as compared with activated carbon, the carbon nanofibers possess smaller interlayer distance.

The texture properties of the carbon materials were investigated with  $\text{N}_2$  adsorption-desorption isotherm. As seen in Figure S11 (Supporting Information), an obvious hysteresis loop could be found in the isotherm of  $\text{C}_{\text{NP}-500}$  and  $\text{C}_{\text{NP}-600}$ , which strongly suggests the mesoporous nature of the carbon materials. The specific surface area of these two materials is  $\approx 50\text{ m}^2\text{ g}^{-1}$ . The relatively low area might be caused by a relatively compact contact between the nanofibers. For example, the specific surface area of the single-walled carbon nanotubes could drop from 1315 to  $151\text{ m}^2\text{ g}^{-1}$  when 217 nanotubes form a bundle, and the surface area would further be smaller by increasing the number of nanotube units in the bundle.<sup>[20]</sup> Moreover, for  $\text{C}_{\text{NP}-700}$ , the isotherm completely changed to type II, which is corresponding to the non-porous texture, and the corresponding specific surface area severely declines to  $\approx 7\text{ m}^2\text{ g}^{-1}$ . In sum, the texture properties match with the results of SEM and TEM characterizations very well.

## 2.4. $\text{Pt}_1@ \text{C}_{\text{NP}-600}$ Catalyst Synthesis and Characterization

With rich heteroatom doping/functional groups,  $\text{C}_{\text{NP}-600}$  has great potential as a carbon support for catching and stabilizing single atoms. The  $\text{C}_{\text{NP}-600}$  was grafted with Pt atoms:  $\text{H}_2\text{PtCl}_6$  was mixed with ethanol, water, and  $\text{C}_{\text{NP}-600}$ , and stirred for 48 h at room temperature. Ethanol was chosen for the

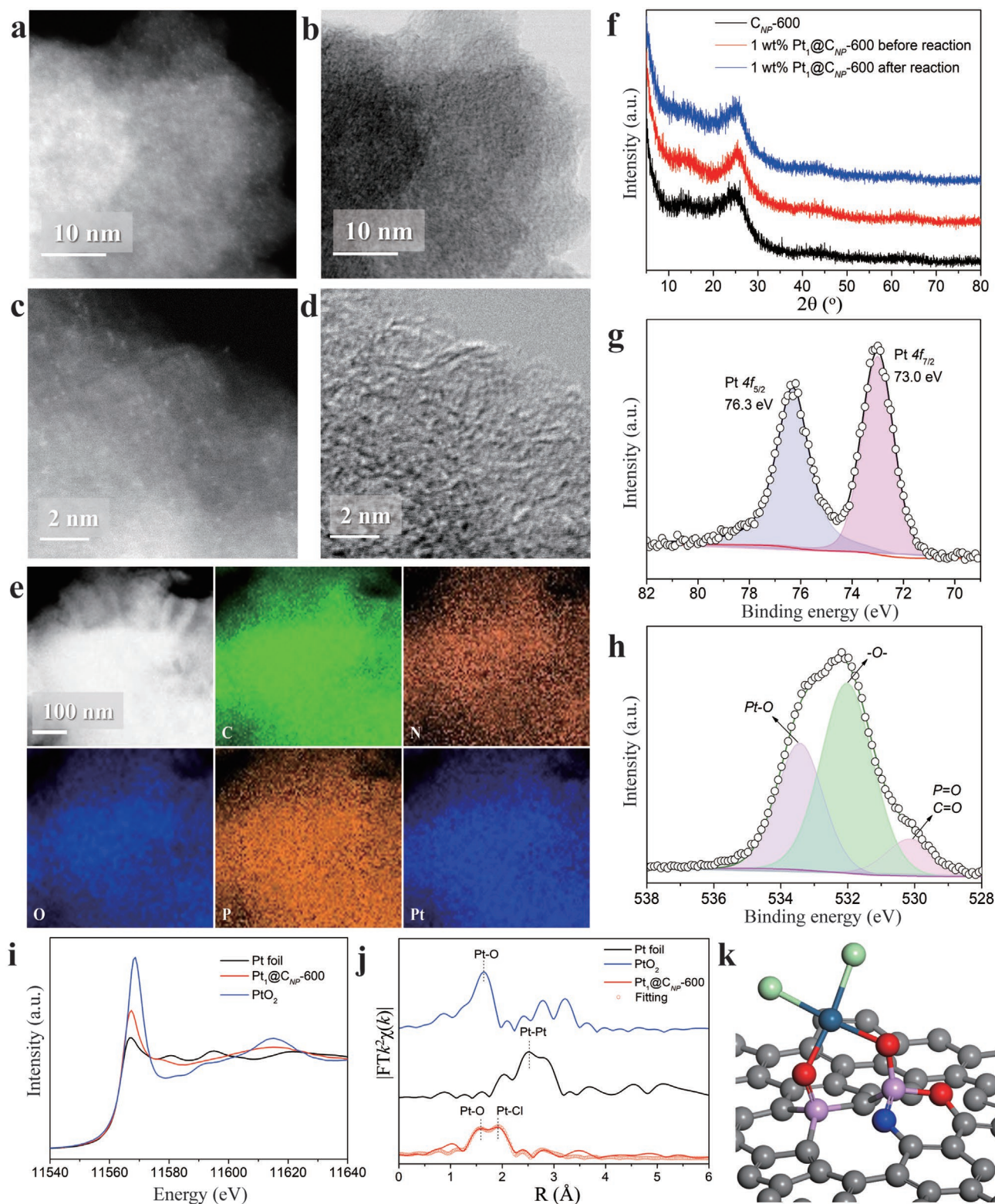
reduction of  $\text{H}_2\text{PtCl}_6$ . After that, the catalyst was filtrated, washed, and vacuum dried at  $60\text{ }^\circ\text{C}$  for 24 h. Inductively coupled plasma optical emission spectroscopy shows the Pt loading is 1 wt%, which is corresponding to the amount of  $\text{H}_2\text{PtCl}_6$  precursor used.

A visual appearance is obtained by HRTEM. Figure 4a–d shows high-angle annular dark-field and bright-field scanning HRTEM images of  $\text{Pt}_1@ \text{C}_{\text{NP}-600}$ . As manifested by the bright spots, Pt atoms are found atomically dispersed on  $\text{C}_{\text{NP}-600}$ , sometimes some Pt atoms a little close to each other were seen, which may result from projection overlaps,<sup>[21]</sup> but no Pt nanoparticles were observed. XRD further shows the absence of any peak corresponding to Pt nanoparticles, indicating the perfect dispersion of Pt on  $\text{C}_{\text{NP}-600}$  (Figure 4f). Elemental mapping of energy-dispersive X-ray spectroscopy (EDX) (Figure 4e) further qualitatively reveals the homogeneous distribution of C/N/O/Pt elements. XPS shows that the  $\text{Pt}_1$  is electron deficient with the  $\text{Pt}4f_{7/2}$  peak at  $73.0\text{ eV}$  (Figure 4g). As shown in Figure 4h and Figure S12 (Supporting Information), after Pt grafting, all the XPS peaks (including N1s, O1s, P2p) shift a little, which may result from the electron transfer between the  $\text{C}_{\text{NP}-600}$  (as a huge ligand) and the  $\text{Pt}_1$  atoms. More importantly, a new prominent peak at  $533.4\text{ eV}$  appeared for the O1s spectrum, which may result from the coordination between O ( $\text{P}=\text{O}/\text{C}=\text{O}$  or  $\text{N}=\text{P}-\text{OH}$ ) and  $\text{Pt}_1$  atoms. Note: for O1s, the  $\text{P}=\text{O}/\text{C}=\text{O}$  peak decreases greatly while P-OH disappears compared to that of  $\text{C}_{\text{NP}-600}$ . Meanwhile, XPS spectra of Cl2p (Figure S12c, Supporting Information) show that some  $\text{Cl}^-$  may still coordinate to  $\text{Pt}_1$  atoms in  $\text{Pt}_1@ \text{C}_{\text{NP}-600}$ . As far as we know, for the coordination of  $\text{Cl}^-$  and unsaturated O ( $\text{C}=\text{O}$ ),  $\text{Pt}_1$  is not so electron deficient (Figure 4g).<sup>[22]</sup> The electron donating ability of the high valence state P to the specific O ( $\text{P}=\text{O}/\text{N}=\text{P}-\text{OH}$ ) is limited, and more electrons will be donated by  $\text{Pt}_1$  atoms to O ( $\text{P}=\text{O}/\text{N}=\text{P}-\text{OH}$ ) for the Pt–O–P coordination. Therefore, the coordination of O is from  $\text{P}=\text{O}/\text{N}=\text{P}-\text{OH}$ .

To gain more information of the electronic and coordination structures of  $\text{Pt}_1$  atoms in  $\text{Pt}_1@ \text{C}_{\text{NP}-600}$ , X-ray absorption near-edge structure (XANES) and Fourier transform-extended X-ray absorption fine structure (FT-EXAFS) spectra were measured. The white-line intensity in sample  $\text{Pt}_1@ \text{C}_{\text{NP}-600}$  is between those of Pt foil and  $\text{PtO}_2$  (Figure 4i), indicating the Pt single atoms in  $\text{Pt}_1@ \text{C}_{\text{NP}-600}$  is electron deficient, which is consistent with the XPS results (Figure 4g). There are two prominent peaks at  $1.58$  and  $1.9\text{ \AA}$  in the FT-EXAFS results (R space, Figure 4j), which are corresponding to the Pt–O and Pt–Cl bonds, respectively.<sup>[23]</sup> For the peak at  $1.58\text{ \AA}$  (Pt–O), it is a little shorter than that for  $\text{PtO}_2$  ( $\approx 1.65\text{ \AA}$ , R space), which may result from the stronger coordination between Pt and O ( $\text{P}=\text{O}/\text{N}=\text{P}-\text{OH}$ ). Based on the XPS and FT-EXAFS results, a schematic model of  $\text{Pt}_1$  coordination environment in 1 wt.%  $\text{Pt}_1@ \text{C}_{\text{NP}-600}$  was given in Figure 4k, and the best curve fitting indicates that  $\text{Pt}_1$  atoms are coordinated by two O and two  $\text{Cl}^-$  (Figure 4j; Table S1, Supporting Information).

**Figure 3.** Characterization of the carbon nanofibers assemblies. a,b) TEM images of the  $\text{C}_{\text{NP}-500}$  (a) and  $\text{C}_{\text{NP}-600}$  (b). c,d) TEM mapping of  $\text{C}_{\text{NP}-500}$  (c) and  $\text{C}_{\text{NP}-600}$  (d), respectively. e–h) XPS characterizations of the  $\text{C}_{\text{NP}-600}$ : e) survey, f) N1s spectrum, g) O1s spectrum, and h) P2p spectrum. i–k) EELS characterizations of the  $\text{C}_{\text{NP}-600}$ : i) C, j) N and k) P. l,m) Solid-state NMR characterizations of the  $\text{C}_{\text{NP}-600}$ : l)  $^{13}\text{C}$  and m)  $^1\text{H}$ .





**Figure 4.** Characterization of 1 wt% Pt<sub>1</sub>@C<sub>NP</sub>-600. a–d) High-angle annular dark-field (a,c) and bright-field (b,d) STEM images and e) EDX mapping of 1 wt% Pt<sub>1</sub>@C<sub>NP</sub>-600. f) XRD patterns of C<sub>NP</sub>-600, 1 wt% Pt<sub>1</sub>@C<sub>NP</sub>-600 and the catalyst after reaction. g,h) XPS spectra: g) Pt 4f spectrum and h) O 1s spectrum of 1 wt% Pt<sub>1</sub>@C<sub>NP</sub>-600; i) Pt L<sub>3</sub>-edge XANES of 1 wt.% Pt<sub>1</sub>@C<sub>NP</sub>-600; and j) FT-EXAFS spectra of 1 wt% Pt<sub>1</sub>@C<sub>NP</sub>-600, Pt foil, and PtO<sub>2</sub>. k) Schematic model of Pt coordination environment in 1 wt.% Pt<sub>1</sub>@C<sub>NP</sub>-600. The red, blue, bright blue, magenta, light green, and gray spheres represent O, Pt, N, P, Cl, and C atoms, respectively.

## 2.5. Catalytic Properties of Pt<sub>1</sub>@C<sub>NP</sub>-600 for Hydrosilylation

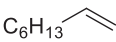
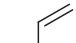
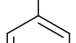
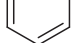

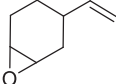
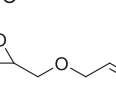
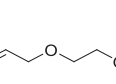
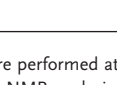
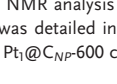
The catalytic ability of Pt<sub>1</sub>@C<sub>NP</sub>-600 was evaluated in hydrosilylation reaction for a wide range for both alkenes and silanes (Table 1). For the benchmark reaction between 1-octene and (Me<sub>3</sub>SiO)<sub>2</sub>MeSiH, C<sub>NP</sub>-600 shows no catalytic ability. However, Pt<sub>1</sub>@C<sub>NP</sub>-600 shows an ultrahigh activity with a high selectivity (99%) (Entry 4, Table 1), indicating single Pt atoms immobilized on the C<sub>NP</sub>-600 should be the real catalytic sites. The TOF is as high as 9.2 × 10<sup>6</sup> h<sup>-1</sup>, which is almost the same to best performance heterogeneous catalyst Pt<sub>1</sub>@AHA\_U\_400 catalyst (9.7 × 10<sup>6</sup> h<sup>-1</sup>).<sup>[22]</sup> Compared to a Karstedt Pt catalyst, no special activation period was needed, and the solution remained colorless and transparent after reaction and separation of the heterogeneous catalyst, indicating high stability of Pt<sub>1</sub>@C<sub>NP</sub>-600 during the hydrosilylation process.<sup>[7,9,24]</sup> Pt<sub>1</sub>@C<sub>NP</sub>-600 showed 100% selectivity for the hydrosilylation of 1,2-epoxy-4-vinylcyclohexane (Entries 13 and 14, Table 1), where opening/polymerization of the sensitive epoxide function is observed when Karstedt catalysts were used.<sup>[7]</sup> Meanwhile, the TOF

values of Pt<sub>1</sub>@C<sub>NP</sub>-600 are 3–10 times higher than that of Pt<sub>1</sub>@AHA\_U\_400 in the hydrosilylation of diverse terminal olefins with functional groups (Entries 5–18, Table 1).<sup>[22]</sup> Meanwhile, the Pt<sub>1</sub>@C<sub>NP</sub>-600 also shows much higher activities than other heterogeneous catalysts when (CH<sub>3</sub>CH<sub>2</sub>O)<sub>3</sub>SiH was used as silane (Entry 6 and 12, Table 1).<sup>[10,25]</sup>

The high activity and selectivity of Pt<sub>1</sub>@C<sub>NP</sub>-600 shows little change even when the catalyst was recycled for six times (Figure S13, Supporting Information), indicating the high stability of the catalyst. STEM images of the spent catalyst show no aggregation of the Pt single atoms (Figure S14, Supporting Information). To further evaluate the stability of Pt<sub>1</sub>@C<sub>NP</sub>-600 catalyst, a Pt leaching test (Entry 3, Table 1) was performed, and the detected Pt concentration in the crude reaction solution is negligible (0.06 ppm, corresponding to about 0.9% of the initial Pt adding amount). At the same time, no conversion was observed by using the crude reaction solution as catalyst, indicating the atomically dispersed Pt on C<sub>NP</sub>-600 are the real catalytic sites.

The ultrahigh activity of Pt<sub>1</sub>@C<sub>NP</sub>-600 catalyst may be attributed to the atomic dispersion of isolated Pt atoms, the electron

**Table 1.** Hydrosilylation of terminal olefins catalyzed by Pt<sub>1</sub>@C<sub>NP</sub>-600.

Entry <sup>a)</sup>	Alkene	Silane	Catalyst [mol%] <sup>b)</sup>	Reaction			TOF [h <sup>-1</sup> ] <sup>c)</sup>
				t min <sup>-1</sup>	T Yield [%]	T selectivity [%]	
1 <sup>d)</sup>		PhMe <sub>2</sub> SiH	1 × 10 <sup>-3</sup>	1	73	>99	4.4 × 10 <sup>6</sup>
2 <sup>d)</sup>		(Me <sub>3</sub> SiO) <sub>2</sub> MeSiH	5 × 10 <sup>-4</sup>	1	44	>99	5.3 × 10 <sup>6</sup>
3		(Me <sub>3</sub> SiO) <sub>2</sub> MeSiH	1.25 × 10 <sup>-3</sup>	1	99	99	4.8 × 10 <sup>6</sup>
4 <sup>d)</sup>		(Me <sub>3</sub> SiO) <sub>2</sub> MeSiH	5 × 10 <sup>-4</sup>	1	77	99	9.2 × 10 <sup>6</sup>
5		(CH <sub>3</sub> CH <sub>2</sub> O) <sub>2</sub> CH <sub>3</sub> SiH	1.7 × 10 <sup>-2</sup>	1	99	>99	4.0 × 10 <sup>5</sup>
6		(CH <sub>3</sub> CH <sub>2</sub> O) <sub>3</sub> SiH	5 × 10 <sup>-3</sup>	30	92	92	3.7 × 10 <sup>4</sup>
7		PhMe <sub>2</sub> SiH	5 × 10 <sup>-3</sup>	1	90	>99	1.1 × 10 <sup>6</sup>
8			1.7 × 10 <sup>-3</sup>	1	85	>99	3.4 × 10 <sup>6</sup>
9			1 × 10 <sup>-3</sup>	1	61	>99	3.7 × 10 <sup>6</sup>
10		(Me <sub>3</sub> SiO) <sub>2</sub> MeSiH	1.7 × 10 <sup>-2</sup>	1	82	82	3.3 × 10 <sup>5</sup>
11			1 × 10 <sup>-2</sup>	1	45	81	2.7 × 10 <sup>5</sup>
12 <sup>e)</sup>		(CH <sub>3</sub> CH <sub>2</sub> O) <sub>3</sub> SiH	5 × 10 <sup>-3</sup>	15	42	>99	3.4 × 10 <sup>4</sup>
13			1.7 × 10 <sup>-2</sup>	1	>99	>99	1.2 × 10 <sup>5</sup>
14		(Me <sub>3</sub> SiO) <sub>2</sub> MeSiH	5 × 10 <sup>-3</sup>	1	33	>99	3.9 × 10 <sup>5</sup>
15		(Me <sub>3</sub> SiO) <sub>2</sub> MeSiH	1.7 × 10 <sup>-2</sup>	1	91	91	3.6 × 10 <sup>5</sup>
16		(Me <sub>3</sub> SiO) <sub>2</sub> MeSiH	5 × 10 <sup>-3</sup>	1	89	91	1.1 × 10 <sup>6</sup>
17		(Me <sub>3</sub> SiO) <sub>2</sub> MeSiH	1.7 × 10 <sup>-2</sup>	1	82	82	3.3 × 10 <sup>5</sup>
18			5 × 10 <sup>-3</sup>	1	85	85	1.0 × 10 <sup>6</sup>

<sup>a)</sup>Experiments were performed at 4 mmol scale: 1 wt.% Pt<sub>1</sub>@C<sub>NP</sub>-600 catalyst, silane/olefin = 1.1 (mol mol<sup>-1</sup>), temperature = 70 °C. The products yield and selectivity were determined by <sup>1</sup>H NMR analysis using *N,N*-dimethylaniline as internal standard; <sup>b)</sup>Based on olefin substrate; <sup>c)</sup>TOF values were calculated based on T yield, and the calculation method was detailed in Figure S15 (Supporting Information); <sup>d)</sup>To eliminate the influence of mass transfer, improve solid-liquid contact and easy to weigh the catalyst, 0.5 wt.% Pt<sub>1</sub>@C<sub>NP</sub>-600 catalyst was used; <sup>e)</sup>Temperature = 60 °C.



deficiency of the Pt<sub>1</sub> atoms and the unique coordination of Pt<sub>1</sub>.<sup>[22]</sup> It is well known that Pt nanoparticles have almost no catalytic ability for hydrosilylation reactions owing to the strong adsorption of silane and olefin reactants on different Pt atoms of Pt nanoparticles.<sup>[22]</sup> The P,N-doped C<sub>NP</sub>-600 provides great number of anchoring sites for Pt single atoms, while at the same time preventing the aggregation of Pt<sub>1</sub> atoms. Meanwhile, strong interactions between the P,N-doped C<sub>NP</sub>-600 (best understood as a heterogeneous P, N-ligand) and the Pt<sub>1</sub> atoms may result in the high electron deficiency of Pt<sub>1</sub> atom with the electron withdrawn of the support (XPS and XANES results). It has been reported that only moderate coordination strength is beneficial for rapid hydrosilylation, and too strong or too weak interactions both decrease the reactivity.<sup>[8]</sup> The electron-deficient Pt<sub>1</sub> atoms of Pt<sub>1</sub>@C<sub>NP</sub>-600 may provide moderate adsorption for reactants or intermediates compared to Pt(0), while the electron deficiency of the Pt<sub>1</sub> center may be beneficial for lowering energy barrier by optimizing the electron structure of the transition state.<sup>[22]</sup> Meanwhile, the Cl ligand can be easily replaced by the reactants (olefin and silane), which may result in the absence of activation period.

### 3. Conclusion

We have successfully synthesized carbon nanofibers with the –P=N– unit in their chemical structure based on the reaction between P<sub>2</sub>O<sub>5</sub> and NMP. Building on the characterization of the intermediates by FTIR and NMR, the possible reaction mechanism involves the formation of oligomers due to the cyclization of ketene species and subsequently the polymerization at elevating temperature. The –P=N– doped carbon nanofibers were functioned as functional support for Pt atom to build a single-atom catalyst for hydrosilylation. The catalyst displays exceptional performance in the hydrosilylation that the TOF can reach as high as 9.2 × 10<sup>6</sup> h<sup>-1</sup>. Moreover, the selectivity of this material is higher than 99%, which promises effective synthesis of targeted product. It is expected that such carbon nanofibers potentially possess superior prospect in other catalysis application, but not limited to hydrosilylation.

### 4. Experimental Section

The relevant information can be found in Supporting Information.

### Supporting Information

Supporting Information is available from the Wiley Online Library or from the author.

### Acknowledgements

We thank MaxPlanck Society and National Natural Science Foundation of China (52204326) for supporting our research.

Open access funding enabled and organized by Projekt DEAL.

### Conflict of Interest

The authors declare no conflict of interest.

### Data Availability Statement

Research data are not shared.

### Keywords

carbon nanofibers, hydrosilylation, –P=N– doping, single atoms, phosphorus pentoxide

Received: October 10, 2022  
Revised: December 26, 2022  
Published online: March 4, 2023

- [1] S. Iijima, *Nature* **1991**, 354, 56.
- [2] a) X. Gu, W. Qi, S. Wu, Z. Sun, X. Xu, D. Su, *Catal. Sci. Technol.* **2014**, 4, 1730; b) Y. Wu, X. Zhao, Y. Shang, S. Chang, L. Dai, A. Cao, *ACS Nano* **2021**, 15, 7946.
- [3] a) Y. Lv, X. Wu, H. Lin, J. Li, H. Zhang, J. Guo, D. Jia, H. Zhang, *Small* **2021**, 17, 2006442; b) A. Modak, R. Mohan, K. Rajavelu, R. Cahan, T. Bendikov, A. Schechter, *ACS Appl. Mater. Interfaces* **2021**, 13, 8461; c) K. Dong, J. Liang, Y. Wang, Z. Xu, Q. Liu, Y. Luo, T. Li, L. Li, X. Shi, A. M. Asiri, Q. Li, D. Ma, X. Sun, *Angew. Chem., Int. Ed.* **2021**, 60, 10583; d) B. Gholipour, S. Shojaei, S. Rostamnia, M. R. Naimi-Jamal, D. Kim, T. Kavetsky, N. Nouruzi, H. W. Jang, R. S. Varma, M. Shokouhimehr, *Green Chem.* **2021**, 23, 6223; e) X. Liu, L. Dai, *Nat. Rev. Mater.* **2016**, 1, 16064.
- [4] J. Chang, C. Yu, X. Song, X. Tan, Y. Ding, Z. Zhao, J. Qiu, *Angew. Chem., Int. Ed.* **2021**, 60, 3587.
- [5] a) J. L. Speier, J. A. Webster, G. H. Barnes, *J. Am. Chem. Soc.* **1957**, 79, 974; b) B. Karstedt, US3775452A, **1971**.
- [6] a) L. N. Lewis, J. Stein, Y. Gao, R. E. Colborn, G. Hutchins, *Platin. Met. Rev.* **1997**, 41, 66; b) B. Marciniec, *Coord. Chem. Rev.* **2005**, 249, 2374.
- [7] a) I. E. Markó, S. Stérin, O. Buisine, G. Mignani, P. Branlard, B. Tinant, J.-P. Declercq, *Science* **2002**, 298, 204; b) A. M. Tondreau, C. C. H. Atienza, K. J. Weller, S. A. Nye, K. M. Lewis, J. G. P. Delis, P. J. Chirik, *Science* **2012**, 335, 567.
- [8] T. K. Meister, K. Riener, P. Gigler, J. Stohrer, W. A. Herrmann, F. E. Kühn, *ACS Catal.* **2016**, 6, 1274.
- [9] J. Stein, L. N. Lewis, Y. Gao, R. A. Scott, *J. Am. Chem. Soc.* **1999**, 121, 3693.
- [10] Y. Chen, S. Ji, W. Sun, W. Chen, J. Dong, J. Wen, J. Zhang, Z. Li, L. Zheng, C. Chen, Q. Peng, D. Wang, Y. Li, *J. Am. Chem. Soc.* **2018**, 140, 7407.
- [11] L. Zhang, X. Li, M. Antonietti, *Angew. Chem., Int. Ed.* **2021**, 60, 24257.
- [12] a) H. Akbaş, *J. Mol. Struct.* **2020**, 1200, 127079; b) M. Bolboacă, T. Stey, A. Murso, D. Stalke, W. Kiefer, *Appl. Spectrosc.* **2003**, 57, 970; c) R. Sydam, M. Deepa, *J. Mater. Chem. C* **2013**, 1, 7930.
- [13] A. A. Ibrahim, P.-H. Wei, G. D. Harzmann, D. Nalla, M. Mondal, K. A. Wheeler, N. J. Kerrigan, *Tetrahedron* **2021**, 78, 131838.
- [14] J. Liang, J. Chen, H. Shen, K. Hu, B. Zhao, J. Kong, *Chem. Mater.* **2021**, 33, 1789.
- [15] P. Vassileva, V. Krastev, L. Lakov, O. Peshev, *J. Mater. Sci.* **2004**, 39, 3201.
- [16] D. Kepaptsoglou, T. P. Hardcastle, C. R. Seabourne, U. Bangert, R. Zan, J. A. Amani, H. Hofsäss, R. J. Nicholls, R. M. D. Brydson, A. J. Scott, Q. M. Ramasse, *ACS Nano* **2015**, 9, 11398.

- [17] S. Bhattacharyya, M. Lübke, P. R. Bressler, D. R. T. Zahn, F. Richter, *Diam. Relat. Mater.* **2002**, *11*, 8.
- [18] A. Favron, E. Gauffrès, F. Fossard, A.-L. Phaneuf-L'Heureux, N. Y. W. Tang, P. L. Lévesque, A. Loiseau, R. Leonelli, S. Francoeur, R. Martel, *Nat. Mater.* **2015**, *14*, 826.
- [19] a) S. P. Koenig, R. A. Doganov, H. Schmidt, A. H. Castro Neto, B. Özyilmaz, *Appl. Phys. Lett.* **2014**, *104*, 103106; b) T. Dennenwaldt, *Ph.D. degree*, Ludwig-Maximilians-Universität München, Munich, Germany **2013**.
- [20] A. Peigney, C. Laurent, E. Flahaut, R. R. Bacsa, A. Rousset, *Carbon* **2001**, *39*, 507.
- [21] R. F. Egerton, P. Li, M. Malac, *Micron* **2004**, *35*, 399.
- [22] K. Liu, B. Badamdorj, F. Yang, M. J. Janik, M. Antonietti, *Angew. Chem., Int. Ed.* **2021**, *60*, 24220.
- [23] Q. Liu, Z. Zhang, *Catal. Sci. Technol.* **2019**, *9*, 4821.
- [24] a) T. Iimura, N. Akasaka, T. Kosai, T. Iwamoto, *Dalton Trans.* **2017**, *46*, 8868; b) T. Troadec, A. Prades, R. Rodriguez, R. Mirgalet, A. Baceiredo, N. Saffon-Merceron, V. Branchadell, T. Kato, *Inorg. Chem.* **2016**, *55*, 8234.
- [25] Y. Zhu, T. Cao, C. Cao, J. Luo, W. Chen, L. Zheng, J. Dong, J. Zhang, Y. Han, Z. Li, C. Chen, Q. Peng, D. Wang, Y. Li, *ACS Catal.* **2018**, *8*, 10004.